Interfacial defect reduction enhances universal power law response in Mo–SiN$_x$ granular metals

Michael P. McGarry ; Simeon J. Gilbert ; Luke Yates ; Melissa L. Meyerson ; Paul G. Kotula ;
William B. Bachman ; Peter A. Sharma ; Jack D. Flicker ; Michael P. Siegal ;
Laura B. Biedermann ✉

Check for updates

View Online   Export Citation

08 August 2024 00:52:19

Interfacial defect reduction enhances universal power law response in Mo–SiN$_x$ granular metals

Michael P. McGarry, [ID] Simeon J. Gilbert, [ID] Luke Yates, [ID] Melissa L. Meyerson, [ID] Paul G. Kotula, [ID]
William B. Bachman, [ID] Peter A. Sharma, [ID] Jack D. Flicker, [ID] Michael P. Siegal, [ID] and Laura B. Biedermann[a] [ID]

AFFILIATIONS

Sandia National Laboratories, Albuquerque, New Mexico 87185, USA

[a]Author to whom correspondence should be addressed: lbieder@sandia.gov

ABSTRACT

Granular metals (GMs), consisting of metal nanoparticles separated by an insulating matrix, frequently serve as a platform for fundamental electron transport studies. However, few technologically mature devices incorporating GMs have been realized, in large part because intrinsic defects (e.g., electron trapping sites and metal/insulator interfacial defects) frequently impede electron transport, particularly in GMs that do not contain noble metals. Here, we demonstrate that such defects can be minimized in molybdenum–silicon nitride (Mo–SiN$_x$) GMs via optimization of the sputter deposition atmosphere. For Mo–SiN$_x$ GMs deposited in a mixed Ar/N$_2$ environment, x-ray photoemission spectroscopy shows a 40%–60% reduction of interfacial Mo-silicide defects compared to Mo–SiN$_x$ GMs sputtered in a pure Ar environment. Electron transport measurements confirm the reduced defect density; the dc conductivity improved (decreased) by 10^4–10^5 and the activation energy for variable-range hopping increased 10×. Since GMs are disordered materials, the GM nanostructure should, theoretically, support a universal power law (UPL) response; in practice, that response is generally overwhelmed by resistive (defective) transport. Here, the defect-minimized Mo–SiN$_x$ GMs display a superlinear UPL response, which we quantify as the ratio of the conductivity at 1 MHz to that at dc, $\Delta\sigma_\omega$. Remarkably, these GMs display a $\Delta\sigma_\omega$ up to 10^7, a three-orders-of-magnitude improved response than previously reported for GMs. By enabling high-performance electric transport with a non-noble metal GM, this work represents an important step toward both new fundamental UPL research and scalable, mature GM device applications.

I. INTRODUCTION

Granular metals (GMs) are three-dimensional (3D) composites of metal nanoparticles dispersed within an insulating matrix, whose composition, volumetric metal fraction, and growth environment enable control over electron transport. Granular metals are useful for fundamental transport mechanism studies, including percolation theory,[1,2] variable-range hopping,[1,3] Coulomb interactions,[4,5] giant magnetoresistance,[6] and the universal power law (UPL) response.[7–10] The potential utility of GMs has also sparked interest in applications including electric-field (E-field) and strain-sensing devices,[11,12] tunnel barriers for nanoelectronics,[13] high-frequency magnetic devices,[14] and plasmonic sensors.[15,16]

However, despite over 50 years of investigation into GMs, few, if any, commercial devices incorporating GMs have been realized; at present, there are two minor challenges and one significant challenge. First, scaling up the conventional co-sputter deposition process is nontrivial; however, sputtering is commonly used for commercial microelectronics and solar-cell fabrications.[17] Second, desirable electron transport properties are more frequently observed in GMs containing noble metals, increasing costs for GM devices. Most problematically, defects are introduced during the GM growth process (e.g., electron trapping sites and interfacial defects) that impede transport in otherwise technologically advantageous GMs, including Ni–SiO$_2$, Co–ZrO$_2$, and Co–YSZ (yttria-stabilized zirconia).[18] To address this third challenge, we recently demonstrated a method to reduce interfacial defects and improve (lower) dc conductivity for Mo- and Co-containing GMs by using a silicon nitride insulating matrix, rather than a conventional oxide insulating matrix.[19] Parallel work in ac transport measurements also showcased the utility of other non-oxide GMs, such as Pt–C,[11] Co–BaF$_2$,[20] and Co–SiN$_x$.[21] However, to sufficiently reduce defects

and enable the performance required for functional devices, better synthesis processes are needed.

Conventionally, GMs are co-sputter deposited in inert Ar environments. However, a few reports have shown that altering the deposition environment to include the gas that defines the insulating matrix (e.g., O_2 for Pt–SiO_2[7] and N_2 for Co–SiN_x[21]) robustly decreases defect formation. To evaluate the chemical and electronic benefits of this matched synthesis environment with a more-reactive refractory metal,[19] we co-sputtered Mo–SiN_x GMs in two environments, pure Ar and partial N_2/forming gas. Forming gas (97% Ar, 3% H_2) was chosen over pure Ar to scavenge trace oxygen. We then extensively characterized the resulting materials to compare their respective defect formation states, activation energy (as a proxy for insulator defect density), and high E-field response (to show the presence of any Fowler–Nordheim and trap-assisted Poole–Frenkel type tunneling). Finally, ac transport measurements assessed the UPL response of Mo–SiN_x at room temperature. Theoretically, all disordered materials, including GMs, should support a UPL response.[10,22] However, prior evaluations of Pd–ZrO_2 and Pt–C GMs showed distinct UPL responses only at cryogenic temperatures; at room temperatures, the UPL response was generally overwhelmed by resistive (defective) transport.[9,11]

Materials having strongly non-linear ac transport and high E-field strength are desired for high-pass filter elements in shunt devices to divert deleterious ultrafast transients while withstanding high-voltage operating conditions. In the specific case of Mo–SiN_x GMs, reducing defect formation to simultaneously maximize high E-field strength and UPL response may be the critical next step toward commercially viable granular-metal based shunt devices.

II. EXPERIMENT

A. Mo–SiN_x GM synthesis

To analyze metal fraction (φ)-dependent GM conduction, we prepared Mo–SiN_x thin film samples with $0.2 < \varphi < 0.8$. The notation SiN_x indicates known nitrogen vacancies that occur in sputtered Si_3N_4 films, such as those sputtered in a pure Ar atmosphere.[19,23,24] The samples were synthesized via rf co-sputtering of Mo targets (ACI Alloys) and Si_3N_4 targets (Plasmaterials). For electrical and x-ray photoemission spectroscopy (XPS) measurements, GM films were grown on highly insulating 10×10 mm^2 sapphire substrates with a 20 nm SiN_x capping layer to prevent oxidation of the nanoparticles. For initial material testing, we followed our previously established procedure to produce a "100% Ar" sample batch of 100 nm-thick GM films sputtered in a 5 mTorr Ar atmosphere.[19] Then, to improve performance and material quality, we modified this method to produce additional "10% N_2" sample batches of 200–280 nm-thick GM films (with thickness variance between different batches but uniform for each φ), sputtered in a 5.5 mTorr atmosphere composed of 10% N_2 mixed with 90% forming gas. In the 10% N_2 environment, the SiN_x had a sputtering power of 100 W while the Mo sputtering power ranged from 16 to 51 W depending on the metal fraction desired. For Mo–SiN_x, the deposition rate ranged from 2.0 nm/min for $\varphi = 0.25$ to 3.3 nm/min for $\varphi = 0.60$. Multiple GM samples were sputtered simultaneously for each batch, generating nominally identical samples (as

confirmed by dc electrical tests) for dc and ac electrical testing, as well as XPS analysis. Thin, 5-nm-thick GM films were grown on 20-nm-thick SiO_2 transmission electron microscopy (TEM) grids for scanning TEM (STEM) measurements. The experimental procedures for XPS and STEM measurements were reported in our previous work.[19]

Optical transmission and conductivity (σ) measurements informed our choice of a 10% N_2 environment for GM sputtering. Bandgap calculations from optical transmission measurements of sputtered SiN_x films (see Fig. S1 in the supplementary material), showed an increase in E_{gap} from 100% Ar (4.25 eV) to 10% N_2 (4.8 eV), approaching the stochiometric Si_3N_4 value (5.3 eV).[25] Increasing the N_2 concentration to 50% N_2 resulted in only a slight E_{gap} improvement (4.9 eV). The dc σ (σ_{dc}) for pure SiN_x was 10^{-12} S/cm in both the 100% Ar and 10% N_2 environments. However, high N_2 is detrimental to Mo conductivity. Pure Mo thin films have reported values of σ_{dc} = 2-30 kS/cm.[26–29] Our Mo films sputtered in 100% Ar had σ_{dc} = 7 kS/cm, 10× higher than those sputtered in 10% N_2 (σ_{dc} = 0.6 kS/cm). The Mo σ_{dc} continued to decrease for higher N_2 fractions (see Fig. S2 in the supplementary material). Based on this preliminary work, we chose 10% N_2 as an appropriate concentration to reduce insulator vacancies and secondary phase formation without detrimentally decreasing the nanoparticle σ.

B. Device fabrication and testing

To better reveal the temperature-dependent conductivity $\sigma(T)$, σ_{dc}, and frequency-dependent conductivity $\sigma'(\omega)$ in the samples, we evaluated transport in a variety of setups using three distinct electrode geometries: van der Pauw (vdP), parallel bar, and circular transmission line method (CTLM). Room-temperature low E-field σ_{dc} was assessed using samples having vdP corner electrodes (2×2 mm^2), created using a shadow mask. First, a 400 V Ar-ion mill was used to remove the SiN_x capping layer in the corner electrode regions, and then Ti/Au electrodes (10/100 nm) were deposited *in situ*. The vdP measurements used a Keithley 6221 dc current source with a Keithley 6517B electrometer measuring voltage drop. These low E-field σ_{dc} measurements were conducted with E-fields ≤5 V/cm.

Next, following established literature techniques, we used the parallel bar method to measure $\sigma(T)$.[9,11,30] Parallel bar electrodes were fabricated using conventional photolithography processes. The SiN_x capping layer was removed via reactive-ion etch to allow deposition of Ti/Pt/Au (20/20/300 nm) electrodes; however, to minimize surface conduction, the SiN_x was preserved in the exposed regions between the electrodes. $\sigma(T)$ was obtained using custom-printed circuit boards (PCBs, Rogers 4003); a AuSn solder reflow process adhered the GM sample to the PCB, face-down [see Fig. S3(a) in the supplementary material]. The cryogenic σ_{dc} measurements, 20–300 K, were conducted in a Janis CCS 450 10 K cryostat with a LakeShore model 335 temperature controller. Apiezon N thermal grease applied between the sapphire GM substrate and the copper mounting block inside the cryostat ensured low thermal resistance. A Zurich Instruments lock-in amplifier (5 MHz MFLI) measured the charge carrier response. Thermal sweeps were conducted as two-wire measurements to minimize

cable parasitics; the high and low electrodes were separately shorted at the PCB. Instrumentation constraints limited the minimum measured σ to 10^{-9} S/cm.

Although most GM studies have used parallel bar electrodes for $\sigma'(\omega)$,[8,9,30,31] we followed well-established methods for rf measurements and chose the CTLM geometry,[32] which proved to be highly effective for obtaining both high E-field σ_{dc} measurements and $\sigma'(\omega)$. Using the same photolithography processes described above, we deposited CTLM electrodes with a 2 mm inner radius and a 0.1 mm gap distance [see Fig. S3(b) in the supplementary material]. To avoid surface flashover during the σ_{dc} measurements (conducted with a Keysight B1505A Source Measure Unit), the samples were submersed in Fluorinert FC-70. For $\sigma'(\omega)$ measurements, the CTLM samples were then wire bonded (3×1 mil^2 Au ribbon wire) to a second custom PCB. The CTLM $\sigma'(\omega)$ measurements were conducted on two instruments. To better align with our instruments' optimal frequency and sample impedance range, we measured the sample between 1 Hz and 10 kHz with a Zurich Instruments lock-in amplifier (5 MHz MFLI) and between 10 kHz and 1 MHz with an Agilent 4294A precision impedance analyzer.

III. IMPACT OF SPUTTERING ENVIRONMENT

A. Nanostructure analysis

Figure 1 shows representative high-angle angular dark-field (HAADF) STEM images of Mo–SiN$_x$ GMs grown in 100% Ar and 10% N$_2$/90% forming gas; the bright oblate features are the Mo nanoparticles. Both the nanoparticle diameters and interparticle separations increase monotonically with increasing φ.[19] However, at

each given φ, the Mo nanoparticles within GMs grown in 10% N$_2$ are smaller than those grown in pure Ar. The difference in the nanoparticle size is caused by the increase in total pressure and the inclusion of N$_2$, both of which affect the sputtering kinetics. The relation between the grain size and the total sputtering pressure of metallic films has been extensively studied, with higher pressures corresponding to smaller grains.[27,33,34] Smaller grain sizes form when the sputtered material collides with the deposition gas, which then lowers the kinetic energy and surface mobility of the deposited material.[33] Similar growth patterns were also demonstrated for WO$_3$ and indium tin oxide films; both reported smaller grain sizes for higher N$_2$ partial pressures in Ar/N$_2$ growth environments.[35,36]

B. DC conductivity at low E-fields

1. Influence of sputter atmosphere

GMs have distinct metallic and insulating regimes,[2] corresponding to $\varphi \gtrsim 0.6$ (high φ) and $\varphi \lesssim 0.4$ (low φ) for these Mo–SiN$_x$ GMs.[19] In the high φ regime, the GM is a disordered metal with limited insulator inclusions; thus, the electron transport is linear, following Ohm's law. In the low φ regime, the GM has isolated metal nanoparticles within an insulating matrix; tunneling and variable range hopping (VRH) dominate.[2] Figure 2 compares the σ_{dc} of the Mo–SiN$_x$ GMs as a function of φ for GMs grown in 100% Ar and 10% N$_2$/90% forming gas. For both sets of growth conditions, the general σ_{dc} is typical of GMs: insulating at low φ and conducting at high φ. However, the σ_{dc} increases less acutely from $\varphi = 0.25$ to $\varphi = 1$ for samples grown in 100% Ar (by 10^5) than in 10% N$_2$ (by 10^9). Previously, GMs with the lowest reported σ_{dc} comprised noble metal nanoparticles (Au or Ag) in an insulating oxide matrix.[2] At $\varphi = 0.25$, σ_{dc} of Au and Ag GMs ($\sigma_{dc} = 10^{-5}$–10^{-4} S/cm) outperforms our 100% Ar samples
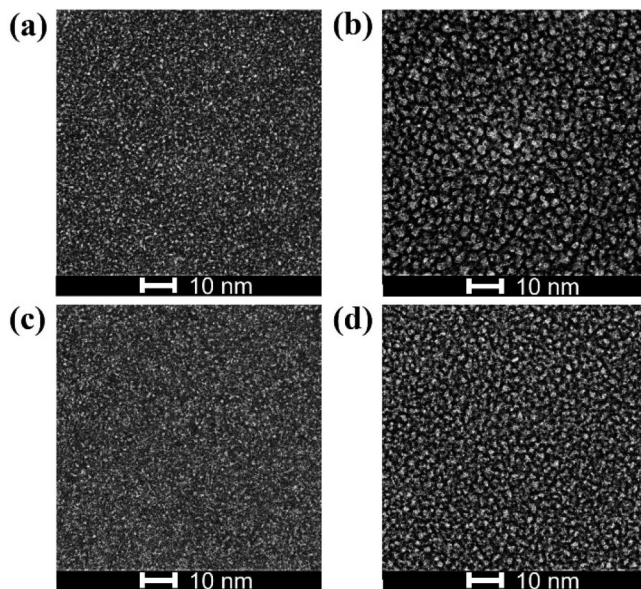

FIG. 1. HAADF STEM images of Mo–SiN$_x$ grown in 100% Ar (a) and (b) and 10% N$_2$ (c) and (d) with $\varphi = 0.2$ (a) and (c) and $\varphi = 0.5$ (b) and (d). The scale bar is 10 nm in all images.
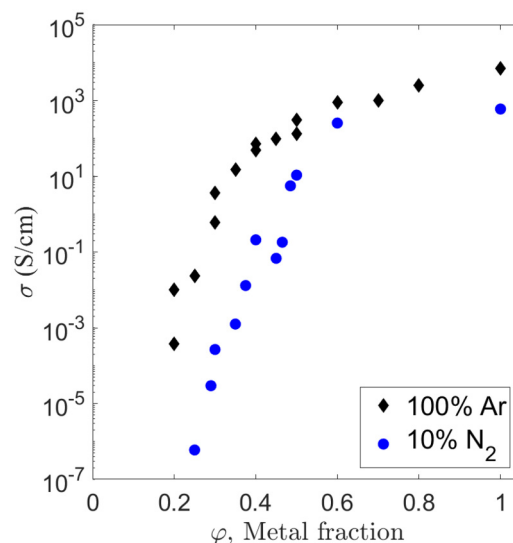

FIG. 2. Dc conductivity for GMs grown in 100% Ar and 10% N$_2$/90% forming gas.

($\sigma_{dc} = 10^{-2}$ S/cm); however, the 10% N_2 samples ($\sigma_{dc} = 10^{-6}$ S/cm) provide σ_{dc} improvements over even noble metal GMs.[2] Considering the $\varphi = 0.25$–0.35 GMs selected for further study, σ_{dc} decreased by $\sim 10^4$–10^5 for GMs sputtered in 10% N_2/90% forming gas. Similarly, sputtering a Co–SiN$_x$ GM in a mixed Ar/N_2 environment, rather than pure Ar, resulted in a $\sim 10^3$ decrease in σ_{dc}.[21]

Unfortunately, depositing these materials in 10% N_2 can lead to Mo-nitride formation, decreasing Mo nanoparticle conductivity, as shown in Fig. 2, where σ_{dc} for pure Mo films deposited in 100% Ar (7 kS/cm) is higher than for pure Mo films deposited in 10% N_2 (0.6 kS/cm). X-ray diffraction (XRD) characterization (see Fig. S4 in the supplementary material) further reveals that for 100% Mo films, Mo-nitride formation increases with increasing N_2. We estimate the impact of Mo-nitride formation by considering the two highest φ samples: $\varphi = 0.6$ and $\varphi = 1$. Since these samples are in the metallic regime, conduction is Ohmic through networks of percolated Mo nanoparticles. Compared to the 100% Ar counterparts, the $\varphi = 0.6$ sample in 10% N_2 is $\sim 3\times$ less conductive, while the $\varphi = 1.0$ sample in 10% N_2 is $\sim 10\times$ less conductive. These σ_{dc} changes may result from Mo-nitride formation; however, in the metallic regime, the decreased nanoparticle sizes (see Sec. III A) may also reduce conductivity due to the increased number of grain boundaries.[27] This slight decrease in Mo nanoparticle conductivity is acceptable for these GMs. From bandgap, σ_{dc}, and XRD studies, we determined the 10% N_2 sputtering atmosphere provides the desired highly insulating SiN$_x$ matrix with minimal nanoparticle degradation.

2. Temperature dependency for charge transport

At low E-fields, GM resistive transport occurs via thermally assisted hopping transport, either VRH or Arrhenius conduction.[4,11] In general, transport in disordered materials is described by Mott's law: $\sigma(T) \sim \exp[-(T_0/T)^\alpha]$, where T_0 is the characteristic temperature, T is temperature, and $\alpha = 0.25$ or 0.5. In GMs, $\alpha = 0.5$ is attributed to thermally activated tunneling between metal nanoparticles.[4,37–39] In VRH, electron hopping (co-tunneling) occurs through multiple nanoparticles, as the transport length exceeds the diameter of a single nanoparticle.[40] The VRH conductivity is given by

$$\sigma_{\text{VRH}}(T) = \sigma_0 \exp\left(-2\sqrt{\frac{E_A}{k_B T}}\right), \quad (1)$$

where σ_0 is a temperature-independent constant, E_A is the activation energy, and k_B is the Boltzmann constant.[11,31] E_A is the energy needed to move an electron between neighboring nanoparticles and is lowered via the presence of insulator defect states.[41] In Arrhenius conduction, the hopping length is on the order of average nanoparticle diameter and only nearest-neighbor hopping occurs. The Arrhenius conduction conductivity is given by

$$\sigma_{\text{Arr}} = \sigma_0 \exp(-\Delta_M/T), \quad (2)$$

where Δ_M is the Coulomb gap between metal nanoparticles.[40] As electronic defects can be partially "frozen out" at low temperatures, some GMs (e.g., Pt/C) exhibit Arrhenius conduction at room
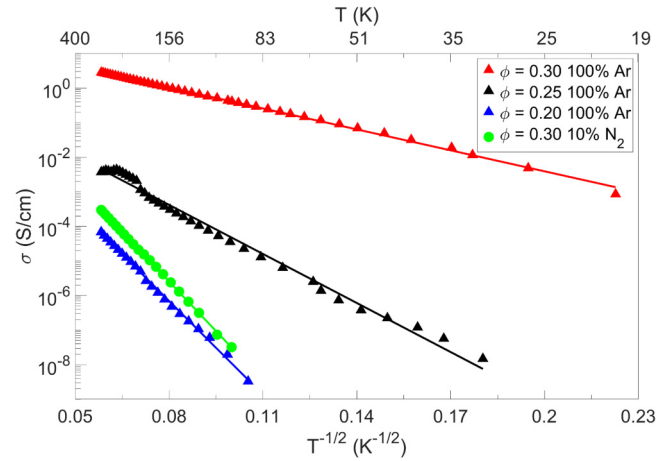

FIG. 3. Conductivity vs $1/T^{1/2}$ for four Mo–SiN$_x$ samples.

temperature and VRH conduction below 175 K.[11] In contrast W–Al$_2$O$_3$ and Ni–SiO$_2$ GMs exhibit VRH from cryogenic temperatures up to 400 K.[38,41]

To examine the low E-field electron transport, we evaluated σ_{dc} of four samples in the low-φ insulating regime at temperatures ranging from 20 to 300 K (Fig. 3). The 100% Ar Mo-SiN$_x$ ($\varphi = 0.3$) sample is the most conductive and showed a three decade decrease in σ_{dc} as the temperature dropped to ~ 20 K; thermally activated charge carriers are progressively frozen-out at decreasing temperatures. Significantly, the three less conductive samples ($\varphi = 0.2$ and 0.25 in 100% Ar and $\varphi = 0.3$ in 10% N_2) showed five to six decade changes in σ_{dc}, characteristic of strongly localized systems.[4] Linear fits of σ to $1/\sqrt{T}$, Eq. (1), show that VRH dominates the electronic transport from 20 to 300 K. As Arrhenius conduction has also been observed for GMs, we further compared the quality of fits for VRH and Arrhenius conduction (see Fig. S5 and Table S1 in the supplemental material). For $\varphi = 0.3$ and 0.35 in 100% Ar, an Arrhenius temperature dependance cannot be fit by a single exponential spanning the measured temperature range, supporting our identification of VRH transport. However, for $\varphi = 0.25$ in 100% Ar and for $\varphi = 0.30$ in 10% N_2, a single Arrhenius exponential also fits the measured temperature range but with lower R^2 value.

From these linear VRH fits, we calculate the E_A for each sample (Table I). The three 100% Ar GMs had E_A values that increase with decreasing φ indicating suppressed tunneling; these E_A are comparable to reported results for Ni–SiO$_2$.[41] For the $\varphi = 0.3$ samples, the E_A was an order of magnitude higher for the 10% N_2 GM (0.84 eV) than the 100% Ar GM (0.078 eV), indicating significant reduction in the defect density within the SiN$_x$, which we then evaluated by XPS. Additionally, the 10% N_2 GM's E_A outperforms the GMs of comparable Ni–SiO$_2$ (0.32 eV at $\varphi = 0.24$) and Pd-ZrO$_2$ (0.013 eV at $\varphi = 0.28$) samples.[9,41]

TABLE I. Activation energies of GMs.

Granular metal	φ	E_A (eV)
Mo-SiN$_x$ (100% Ar)	0.20	1.5
Mo-SiN$_x$ (100% Ar)	0.25	0.22
Mo-SiN$_x$ (100% Ar)	0.30	0.078
Mo-SiN$_x$ (10% N$_2$)	0.30	0.84
Ni-SiO$_2$ (Ref. 38)	0.08	1.1
Ni-SiO$_2$ (Ref. 38)	0.24	0.32
Ni-SiO$_2$ (Ref. 38)	0.44	0.10
Pd-ZrO$_2$ (Ref. 9)	0.28	0.013

C. X-ray photoemission analysis of interfacial defects

To complement these electrical studies, we conducted XPS analysis to quantify the impact of growth conditions on chemical bonding within the GMs. In XPS, binding energies (BEs), and therefore bonding environments, of electrons at surfaces and interfaces are measured. While bandgap measurements indicate that deposition in 10% N$_2$ reduces nitrogen vacancies in the SiN$_x$, introducing N$_2$ into the deposition environment can also result in metal-nitride formation. Thus, our initial goal was to determine whether the Mo-nitride formation was significantly different for the Mo–SiN$_x$ samples grown in 100% Ar and 10% N$_2$. We measured the nitrogen 1s BE in sputtered SiN$_x$ (398.0 eV) and Mo–SiN$_x$ GMs. A reduction of this BE in Mo–SiN$_x$ indicates Mo-nitride formation.[19] The XPS characterization revealed that shifts in the nitrogen 1s BE are more pronounced as φ increases for both the 100% Ar and 10% N$_2$ samples [see Fig. S6(a) in the supplementary material]. However, the difference in nitrogen 1s BEs for 100% Ar and 10% N$_2$ samples is ≤0.1 eV at all φ, suggesting that deposition in 10% N$_2$ did not significantly increase Mo-nitride formation in the Mo–SiN$_x$ GMs. These experimental findings are consistent with the σ_{dc} analysis discussed in Sec. III B.

Our second goal was to determine whether Mo-silicide formation was significantly different for the Mo–SiN$_x$ samples grown in 100% Ar and 10% N$_2$. Mo-silicide formation is indicated by a secondary Si 2p XPS peak at a lower BE (99.3–99.4 eV) than the SiN$_x$ peak (102.2 eV).[19] The BE of this secondary peak is consistent with MoSi$_2$ formation.[42] While this BE is also consistent with pure Si, pure Si is not expected in this system.[19] Relative to the primary SiN$_x$ peak, the area of the Mo-silicide 2p peak increases at higher φ, indicating that Mo-silicide formation increases with greater Mo availability.[19] The area ratio between the two Si 2p XPS peaks was comparable for Mo–SiN$_x$ sputtered in 100% Ar and 10% N$_2$ with the Mo-silicide peak representing 8%–9% of the total peak area at $\varphi = 0.2$ and 33%–39% at $\varphi = 0.6$ [see Fig. S6(b) in the supplementary material]. However, XPS characterization indicates that the Mo/Si atomic ratio was 70%–105% higher when sputtered in 10% N$_2$ [see Fig. S6(c) in the supplementary material] for $\varphi = 0.2$–0.6. Sputtering in N$_2$ increases the nitrogen content in SiN$_x$, meaning that the same volume fraction of SiN$_x$ will have more nitrogen and less Si, increasing the Mo/Si ratio. Assuming all Si atoms associated with the lower-binding-energy Si 2p XPS peak are forming MoSi$_2$, the percent of Mo atoms forming MoSi$_2$ can be
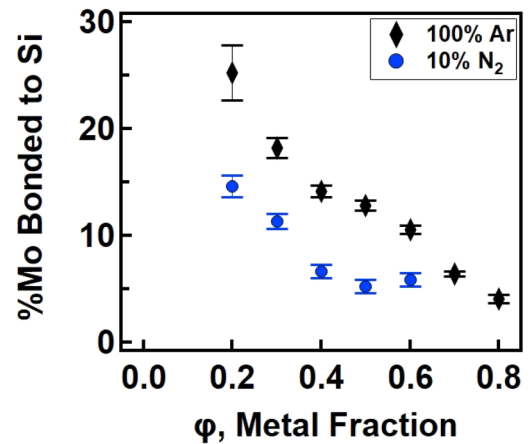

FIG. 4. Calculations from XPS measurements following Eq. (3) showing the decrease of Mo-silicides in Mo–SiN$_x$ GMs sputtered in 10% N$_2$ compared to 100% Ar.

estimated by using Eq. (3), where A_{MoSi_2} is the area of the MoSi$_2$ Si 2p XPS peak divided by the total Si 2p peak area and $R_{Si:Mo}$ is the measured Si:Mo atomic ratio determined by XPS. Based on Eq. (3), there are 40%—60% fewer Mo atoms bound to Si for Mo–SiN$_x$ sputtered in 10% N$_2$ compared to 100% Ar samples (Fig. 4). Thus, the partial N$_2$ growth environment reduces both interfacial MoSi$_2$ defects and defects within the SiN$_x$ insulator, and these changes drive the observed σ_{dc} and E_A improvements,

$$\%\text{Mo bonded to Si} = \frac{1}{2}(A_{MoSi_2} \times R_{Si:Mo}). \quad (3)$$

IV. E-FIELD AND FREQUENCY-DEPENDENT TRANSPORT

A. Field-enhanced tunneling

Since the 10% N$_2$ samples have lower defect densities as determined by the XPS and E_A measurements, we performed high E-field current density vs electric field (J–E) sweeps on these improved samples. These sweeps further highlight the enhanced electrical properties of the GMs by illuminating the role that reduced defect densities have on the relative strength of field-enhanced tunneling. Figure 5 shows three distinct transport regimes—Ohmic transport, Poole–Frenkel type transport, and Fowler–Nordheim tunneling—in J–E measurements. Figure S7 (supplementary material) shows this same data, linearized to highlight these transport regimes. As the spacing between Mo nanoparticles varies within a given GM sample, the E-field is non-uniform, and thus, these transport mechanisms all contribute to the overall sample conductivity.

When the E-field is low, thermally excited emission drives the charge carriers (as evident from VRH temperature dependency, see Sec. III B) and electron transport is defined by simple Ohmic transport for all φ. Classical Poole–Frenkel transport[3,43] dominates
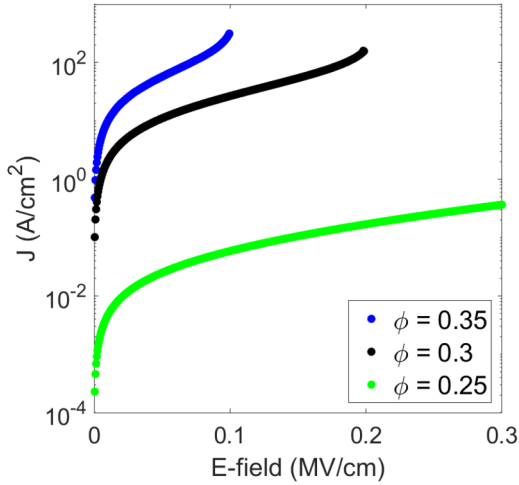
FIG. 5. The J–E characteristics of Mo–SiN$_x$ GMs grown in 10% N$_2$.

when $q\Delta V > k_B T$, where q is charge and ΔV is the voltage drop between the metal nanoparticles. At these moderate E-fields, the GM σ_{dc} exponentially increases via thermally activated defect-assisted tunneling between metal nanoparticles.[3,31] Classical Poole–Frenkel transport is described by[3]

$$\sigma_{PF} \propto \exp\left[(q/k_B T)\sqrt{qE/\mathcal{E}_0 \mathcal{E}_r}\right], \tag{4}$$

where E is the electric field, $\mathcal{E}_0$ is the vacuum permittivity, and $\mathcal{E}_r$ is the high-frequency relative permittivity. Finally, when $q\Delta V$ is greater than the tunneling barrier height, conductivity increases further, as modeled by Fowler–Nordheim tunneling,[31]

$$\sigma_{FN} \propto \exp(E_0/E), \tag{5}$$

where E_0 is a constant. Such Fowler–Nordheim-dominated tunneling has previously been observed in metal–SiO$_2$ GM systems.[44]

Although the $\varphi = 0.25$ sample remains in the Poole–Frenkel type transport regime up to the highest voltages tested (3 kV or 0.3 MV/cm), the $\varphi = 0.30$ and 0.35 samples are dominated by Poole–Frankel-type transport in the moderate E-field regime and Fowler–Nordheim tunneling at higher E-fields, indicated by the measured increase in J (see Figs. 5 and S7 in the supplementary material). In this Fowler–Nordheim regime, electron transport is driven by field-enhanced tunneling through the SiN$_x$ insulating barrier, rather than thermally activated defect-assisted tunneling between metal nanoparticles. As the Mo volume fraction increases, the applied E-field will be further concentrated in the narrow SiN$_x$ insulator regions, resulting in Fowler–Nordheim tunneling dominating at lower applied E-fields. These transport trends are consistent across the temperature range of −50 °C to +125 °C with J increasing monotonically with temperature, as shown in Fig. S8 in the supplementary material. Cooling the GMs reduces the relative contribution from Ohmic and Poole–Frenkel-type transport,

resulting in Fowler–Nordheim tunneling transport dominating at the highest E-fields for all three samples, as shown in Fig. S8 in the supplementary material.

While classical Poole–Frenkel transport has been previously reported for GMs,[43] unambiguously distinguishing between transport mechanisms in disordered materials is challenging. A fundamental assumption of classical Poole–Frenkel transport is that the Coulomb trap separation is sufficient such that the traps are non-interacting, a condition often met in insulators and semiconductors. In disordered and amorphous materials, interactions between traps at high trap densities give rise to the two-activation site Poole–Frenkel (2CPT) transport described by

$$\sigma_{2CPF} \propto \exp[qEa/k_B T], \tag{6}$$

where a is the separation distance between two Coulomb traps.[45,46] The non-interacting classical Poole–Frenkel condition is met at low defect (nanoparticle) densities or high E-fields; the interacting 2CPF condition is met at higher defect (nanoparticle) densities and moderate E-fields. Given these two models for trap-assisted tunneling, we linearized the GM data to both classical Poole–Frankel and 2CPF, as seen in Fig. S7 in the supplementary material. Both Poole–Frankel and 2CPF fit the J–E data well at high E-fields (below the Fowler–Nordheim upturn); at moderate E-fields, 2CPF is a better fit.

B. Superlinear universal power law response

Figure 6 shows the desired strong high-pass frequency response for three Mo–SiN$_x$ samples. As characteristic of disordered materials, the GMs exhibit a σ_{dc} plateau at low ω and a sharply increasing $\sigma'(\omega)$ at high ω (dispersive regime). As φ increases from 0.25 to 0.35, the σ_{dc} plateau increases monotonically. At low ω, resistive transport dominates, corresponding to phase of 0°. As ω increases, the samples enter a dispersive regime; the transition angular frequency increases from 100 Hz to 100 kHz with increasing φ. All three GM samples also exhibit a capacitive response, with phase converging toward −90° at 1 MHz.

To quantify the GM $\sigma'(\omega)$ response, we define the ratio of the conductivity at 1 MHz to that at dc, $\Delta\sigma_\omega$, as

$$\Delta\sigma_\omega = \sigma_{MHz}/\sigma_{dc}, \tag{7}$$

and we calculated $\Delta\sigma_\omega$, Eq. (7), for both Mo–SiN$_x$ and well-characterized literature GMs (Table II). For these various GMs, $\Delta\sigma_\omega$ decreases with increasing φ, as seen in Fig. 6(a) for Mo–SiN$_x$ GMs. While Pd–ZrO$_2$ has a weak $\Delta\sigma_\omega$ ∼50 at room temperature, its $\Delta\sigma_\omega$ increases to ∼500 at 41 K as defective transport is frozen out.[9] Similarly, $\Delta\sigma_\omega$ increased 100× for (FeCoZr)$_{0.52}$(PZT)$_{0.48}$ cooled to 81 K.[47] We observed similar thermal responses in preliminary screening measurements of Mo–SiN$_x$ GMs at cryogenic temperatures. Notably, noble-metal-based Pt–SiO$_2$ has the highest $\Delta\sigma_\omega$, 10^3–10^4, of the oxide-based GMs. In general, noble-metal-based GMs are less likely to form metal-insulator secondary phases.[18] This exceptional Pt–SiO$_2$ $\Delta\sigma_\omega$ was achieved by sputtering in a mixed Ar/O$_2$ environment, where oxygen was introduced to improve silica oxygenation.[7] We propose that the improved SiN$_x$
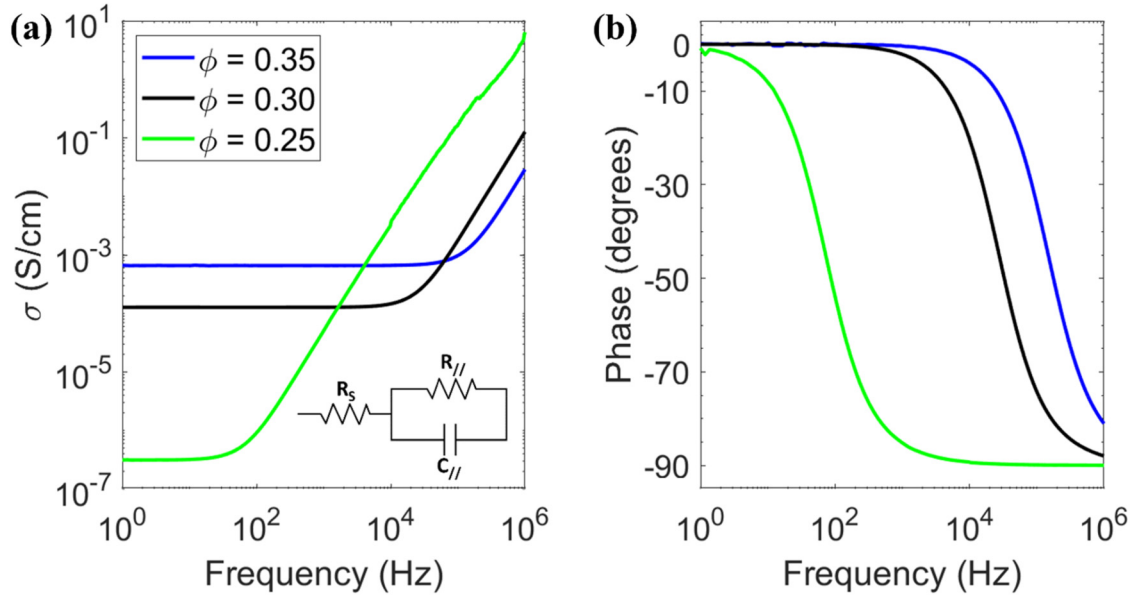
08 August 2024 00:52:19

FIG. 6. (a) Conductivity and (b) phase comparing Mo–SiN$_x$ samples grown in 10% N$_2$. The insert in (a) is the equivalent circuit model for the ω response.

quality obtained in the 10% N$_2$ growth environment enables the extraordinary frequency response of the Mo-SiN$_x$ GMs. Indeed, $\Delta\sigma_\omega$ for $\varphi = 0.25$ GM, $\Delta\sigma_\omega \sim 10^7$, is orders of magnitude higher than anything reported in the literature.

From the measured impedances used to calculate the conductivities in Fig. 6, we used Scribner's Zview software to develop an equivalent circuit model. The Nyquist impedance plots used for model fitting are shown in Fig. S9 in the supplementary material. This GM equivalent circuit model consists of a series resistor R_S, followed by a resistor $R_{//}$ and capacitor $C_{//}$ in parallel. Occasionally, for GMs with weak frequency response, a constant phase element (representing an imperfect capacitor) replaces $C_{//}$.[39] The R_S value includes resistance from percolated nanoparticles and interfacial electrical contact resistance.[11] The parallel circuit element, both $R_{//}$ and $C_{//}$ together, represents the charge transport within the GM sample.[9,30] Ideally, $R_{//}$ is dominated by quantum mechanical tunneling between nanoparticles; Ohmic contributions from defects will decrease $R_{//}$. $R_{//}$ is primarily determined by φ and defect density; $R_{//}$ increases with decreasing T (fewer thermally activated charge carriers) and decreases with applied E-field (field enhanced tunneling). $C_{//}$ reflects the capacitive transport both between the nanoparticles and within the entire system (e.g., GM, SiN$_x$ capping layer, and sapphire substrate). $C_{//}$ is a function of φ, $\mathcal{E}_r$, and nanoparticle size. From the calculated circuit values with $\varphi = 0.25$–0.35 (Table III), we observe that R_S is essentially constant, ~ 1 kΩ, $R_{//}$ decreases exponentially with increasing φ, and $C_{//}$ increases by 0.1 pF from $\varphi = 0.25$ to $\varphi = 0.35$. These observed trends in equivalent circuit values match expected transport models; to first order, the interparticle resistance scales exponentially with nanoparticle separation (tunneling decay length), while the interparticle capacitance is proportional to the nanoparticle diameter.[10]

As for other disordered materials, the $\sigma'(\omega)$ response in GMs follows the empirical universal power law proposed by Jonscher,[9,22,48]

$$\sigma'(\omega) = \sigma_{dc} + A\omega^n,\qquad(8)$$

where A and n are temperature-dependent empirical fitting parameters and n is frequency-dependent as well.[5,9,10,49] Analytical

TABLE II. Table of the room temperature $\Delta\sigma_\omega$ for Mo–SiN$_x$ and literature samples.

Granular metal	φ	ω-range (Hz)	$\Delta\sigma_\omega$
Mo-SiN$_x$ (10% N$_2$)	0.25	10–1 × 10^6	2 × 10^7
Mo-SiN$_x$ (10% N$_2$)	0.30	10–1 × 10^6	1 × 10^3
Mo-SiN$_x$ (10% N$_2$)	0.35	10–1 × 10^6	40
Pd-ZrO$_2$ (Ref. 9)	0.28	10–1 × 10^6	50
Pt-SiO$_2$ (Ref. 7)	0.30	10–1 × 10^6	1 × 10^4
Pt-SiO$_2$ (Ref. 7)	0.60	10–1 × 10^6	1 × 10^3
(FeCoZr)$_{0.52}$(PZT)$_{0.48}$ (Ref. 43)	0.52	50–1 × 10^6	30

TABLE III. Equivalent circuit model parameters and UPL exponent, n.

	R_S (Ω)	$R_{//}$ (Ω)	$C_{//}$ (pF)	n
$\varphi = 0.25$	$\sim 0.2 \times 10^{3a}$	$(1.2 \pm 0.005) \times 10^9$	1.86 ± 0.002	1.56
$\varphi = 0.30$	$(1.6 \pm 0.1) \times 10^3$	$(3.0 \pm 0.001) \times 10^6$	1.93 ± 0.001	1.87
$\varphi = 0.35$	$(1.3 \pm 0.1) \times 10^3$	$(540 \pm 0.1) \times 10^3$	1.99 ± 0.001	1.96

[a]For $\varphi = 0.25$, the ratio of the R_S vs $R_{//}$ value hinders extraction of an exact R_S.

models and numerical simulations show that n relates to the conductance and distribution of conducting paths in disordered materials; n increases with decreasing spread in conducting path lengths (more ordered systems).[10,50] Long path lengths permit resistive transport via VRH; short paths contribute to capacitive transport.[10,51] Superlinear ($n > 1$) $\sigma'(\omega)$ responses have been previously reported in As_2Se_3, mixed alkali glass systems, ferroelectric congruent $LiNbO_3$, conducting polymer chains, and references therein.[22,50,52–54] For a nano-granular metal comprising Pt nanoparticles embedded in an amorphous carbon matrix via e-beam deposition, $n > 2$ was reported.[11] Applying a power-law fit to the measured conductivity [Fig. 6(a)] in the high-frequency dispersive regime, we find that n increases with increasing φ, as noted in Table III. This increase in n suggests that the Mo–SiN_x GMs are becoming more ordered at higher φ. Comparing the STEM images for $\varphi = 0.2$ and $\varphi = 0.5$ (Fig. 1), we qualitatively observe more uniformly short separation distances between Mo nanoparticles at higher φ.

For the $\varphi = 0.25$ Mo–SiN_x sample, a slight decrease in the conductivity slope in the dispersive regime occurs at $\sim 0.1\,MHz$. Multiple origins for this slope decrease are possible. First, the presence of contact and interparticle resistance sets the minimum R_s, limiting the maximum conductivity. Hanefeld et al. attributed a nano-granular metal impedance plateau at $\sim 1\,MHz$ to series resistances.[11] However, the existence of series resistances is not a necessary condition for conductivity saturation. An alternative explanation is that the observed conductivity slope decrease indicates high-frequency saturation, which has been observed in other disordered materials (e.g., Pt/C and conducting polypyrrole).[11,50] Future temperature-dependent frequency-response measurements will evaluate the mechanisms for conductivity saturation.

The strong UPL response of Mo–SiN_x GMs may enable future incorporation in high-power solid-state shunt devices to redirect high-frequency transients to ground. Molybdenum, a refractory metal, is thermally stable and used for electrical contacts in power electronic devices. Silicon nitride has a high breakdown strength, $E_{BD} \sim 10\,MV/cm$, and is frequently used as a passivation layer for microelectronics.[55,56] The strong frequency-dependent conductivity of Mo–SiN_x GMs, as exemplified by their superlinear UPL response, is ideal for such shunt devices. The dc conductivity plateau defines a low-frequency regime in which the Mo–SiN_x GMs are highly insulating, preventing current leakage. In the high-frequency dispersive regime, the now-conductive Mo–SiN_x GMs would shunt nanosecond voltage spikes to ground.

V. CONCLUSIONS

This work demonstrates that sputtering Mo–SiN_x in a partial N_2 environment improves the insulator quality by reducing nitrogen vacancies and Mo-silicide defects, significantly improving GM quality in the tunneling-dominated insulating regime. As benchmarks, we evaluated three GM properties: σ_{dc}, E_A, and $\Delta\sigma_\omega$. For similar φ, we find that Mo–SiN_x is superior to reported GM values in each benchmark. Compared to previously reported results,[19] the dc transport study (σ_{dc} and E_A) showed orders-of-magnitude improvement for SiN_x-based GMs grown in a partial N_2 environment. The combination of insulator and interfacial improvements

enables both high E-field tunneling transport and extraordinarily high $\Delta\sigma_\omega$, three orders of magnitude greater than prior reports. Such Mo–SiN_x GMs provide a well-controlled platform to explore superlinear ac conductivity in disordered materials. This reported growth environment optimization should drive GM synthesis improvements in other GM families, including those with oxide insulators, further advancing transport studies and application development.

SUPPLEMENTARY MATERIAL

See the supplementary material for SiN_x bandgap measurements, conductivity of Mo films sputtered in varying Ar/N_2 environments, optical micrographs of device geometries, XRD of Mo films, additional XPS analysis of the N 1s binding environment Mo-silicide binding, a comparison of VRH and Arrhenius conductivity mechanisms, linearized J–V curves highlighting various transport regimes, temperature-dependent J–E curves, and Nyquist impedance plots.

AUTHOR DECLARATIONS

Conflict of Interest

The authors have no conflicts to disclose.

Author Contributions

Michael P. McGarry: Formal analysis (equal); Investigation (lead); Writing – original draft (lead). **Simeon J. Gilbert:** Formal analysis (equal); Investigation (lead); Writing – review & editing (equal). **Luke Yates:** Investigation (equal); Writing – review & editing (supporting). **Melissa L. Meyerson:** Investigation (equal); Writing – review & editing (supporting). **Paul G. Kotula:** Investigation

(equal); Writing – review & editing (supporting). **William B. Bachman:** Resources (equal); Software (equal). **Peter A. Sharma:** Formal analysis (supporting); Supervision (supporting); Writing – review & editing (equal). **Jack D. Flicker:** Investigation (equal); Writing – review & editing (supporting). **Michael P. Siegal:** Conceptualization (equal); Supervision (equal); Writing – review & editing (equal). **Laura B. Biedermann:** Conceptualization (lead); Formal analysis (equal); Funding acquisition (lead); Supervision (lead); Writing – original draft (lead); Writing – review & editing (lead).

DATA AVAILABILITY

The data that support the findings of this study are available within the article and its supplementary material.

REFERENCES

[1] B. Abeles, H. L. Pinch, and J. I. Gittleman, Phys. Rev. Lett. **35**(4), 247–250 (1975).

[2] C. Grimaldi, Phys. Rev. B **89**(21), 214201 (2014).

[3] J. J. Hauser, Phys. Rev. B **7**(9), 4099–4111 (1973).

[4] A. W. Fung, Z. H. Wang, M. S. Dresselhaus, G. Dresselhaus, R. W. Pekala, and M. Endo, Phys. Rev. B **49**(24), 17325–17335 (1994).

[5] J. C. Dyre and T. B. Schrøder, Rev. Mod. Phys. **72**(3), 873–892 (2000).

[6] D. Kechrakos and K. N. Trohidou, J. Appl. Phys. **89**(11), 7293–7295 (2001).

[7] N. Moyo and K. Leaver, J. Phys. D: Appl. Phys. **13**(8), 1511 (1980).

[8] B. J. Hattink, A. Labarta, M. García del Muro, X. Batlle, F. Sánchez, and M. Varela, Phys. Rev. B **67**(3), 033402 (2003).

[9] H. Bakkali, M. Dominguez, X. Batlle, and A. Labarta, Sci. Rep. **6**, 29676 (2016).

[10] L. Merle, A. Delpoux, A. Mlayah, and J. Grisolia, J. Appl. Phys. **132**(1), 015107 (2022).

[11] M. Hanefeld, P. Gruszka, and M. Huth, Sci. Rep. **11**(1), 15163 (2021).

[12] M. Huth, J. Appl. Phys. **107**(11), 113709 (2010).

[13] X. Luo, M. Tomcsanyi, A. O. Orlov, T. H. Kosel, and G. L. Snider, Appl. Phys. Lett. **89**(4), 043511 (2006).

[14] D. V. Harburg, A. J. Hanson, J. Qiu, B. A. Reese, J. D. Ranson, D. M. Otten, C. G. Levey, and C. R. Sullivan, IEEE J. Emerg. Sel. Top. Power Electron. **6**(3), 1280–1294 (2018).

[15] N. M. Figueiredo, T. Kubart, J. A. Sanchez-García, R. Escobar Galindo, A. Climent-Font, and A. Cavaleiro, J. Appl. Phys. **115**(6), 063512 (2014).

[16] H. Bakkali, E. Blanco, M. Dominguez, M. B. de la Mora, C. Sánchez-Aké, and M. Villagrán-Muniz, Appl. Surf. Sci. **405**, 240–246 (2017).

[17] J. T. Gudmundsson, Plasma Sources Sci. Technol. **29**(11), 113001 (2020).

[18] S. J. Gilbert, S. G. Rosenberg, P. G. Kotula, T. G. Kmieciak, L. B. Biedermann, and M. P. Siegal, J. Phys.: Condens. Matter **34**(20), 204007 (2022).

[19] S. J. Gilbert, M. L. Meyerson, P. G. Kotula, S. G. Rosenberg, T. G. Kmieciak, M. P. McGarry, M. P. Siegal, and L. B. Biedermann, Nanotechnology **34**(41), 415706 (2023).

[20] Y. Cao, N. Kobayashi, C. Wang, S. Takahashi, S. Maekawa, and H. Masumoto, Adv. Electron. Mater. **9**(6), 2201218 (2023).

[21] T. Uchiyama, Y. Cao, H. Kijima-Aoki, K. Ikeda, N. Kobayashi, S. Ohnuma, and H. Masumoto, IEEE Trans. Magn. **59**(11), 1–5 (2023).

[22] P. Lunkenheimer and A. Loidl, Phys. Rev. Lett. **91**(20), 207601 (2003).

[23] M. Vila, C. Prieto, P. Miranzo, M. I. Osendi, and R. Ramírez, Surf. Coat. Technol. **151–152**, 67–71 (2002).

[24] M. Vila, C. Prieto, and R. Ramírez, Thin Solid Films **459**(1–2), 195–199 (2004).

[25] J. Robertson, J. Vac. Sci. Technol. B **18**(3), 1785 (2000).

[26] P. Chelvanathan, Z. Zakaria, Y. Yusoff, M. Akhtaruzzaman, M. M. Alam, M. A. Alghoul, K. Sopian, and N. Amin, Appl. Surf. Sci. **334**, 129–137 (2015).

[27] G. Gordillo, F. Mesa, and C. Calderón, Braz. J. Phys. **36**(3b), 982–985 (2006).

[28] C. Guillén and J. Herrero, J. Mater. Process. Technol. **143–144**, 144–147 (2003).

[29] Y. K. Ko, D. S. Park, B. S. Seo, H. J. Yang, H. J. Shin, J. Y. Kim, J. H. Lee, W. H. Lee, P. J. Reucroft, and J. G. Lee, Mater. Chem. Phys. **80**(2), 560–564 (2003).

[30] B. Hattink, M. García del Muro, Z. Konstantinovic, V. Puntes, X. Batlle, A. Labarta, and M. Varela, Int. J. Nanotechnol. **2**(1–2), 43–61 (2005).

[31] B. Abeles, P. Sheng, M. D. Coutts, and Y. Arie, Adv. Phys. **24**(3), 407–461 (1975).

[32] W. H. de Jeu, R. W. J. Geuskens, and G. E. Pike, J. Appl. Phys. **52**(6), 4128–4134 (1981).

[33] J. A. Thornton, J. Vac. Sci. Technol. **11**(4), 666–670 (1974).

[34] K. Y. Chan and B. S. Teo, IET Sci. Meas. Technol. **1**(2), 87–90 (2007).

[35] A. K. Chawla, S. Singhal, H. O. Gupta, and R. Chandra, Thin Solid Films **518**(5), 1430–1433 (2009).

[36] Z. Liu, J. Liang, H. Zhou, J. Li, M. Yang, S. Cao, and J. Xu, Ceram. Int. **48**(9), 12924–12931 (2022).

[37] I. A. Svito, A. K. Fedotov, A. Saad, P. Zukowski, and T. N. Koltunowicz, J. Alloys Compd. **699**, 818–823 (2017).

[38] I. Balberg and J. Jedrzejewski, Appl. Phys. Lett. **106**(14), 143103 (2015).

[39] H. Bakkali, M. Dominguez, X. Batlle, and A. Labarta, J. Phys. D: Appl. Phys. **48**(33), 335306 (2015).

[40] I. S. Beloborodov, A. V. Lopatin, V. M. Vinokur, and K. B. Efetov, Rev. Mod. Phys. **79**(2), 469–518 (2007).

[41] P. Sheng, B. Abeles, and Y. Arie, Phys. Rev. Lett. **31**(1), 44–47 (1973).

[42] R. S. Rastogi, V. D. Vankar, and K. L. Chopra, J. Vac. Sci. Technol. A **10**(4), 2822–2825 (1992).

[43] B. Abeles, *Applied Solid State Science* (Elsevier, 1976), Vol. 6, pp. 1–117.

[44] C. Falcony, D. J. DiMaria, and C. R. Guarnieri, J. Appl. Phys. **53**(7), 5347–5349 (1982).

[45] A. Bourgine, J. Grisolia, M. Vallet, D. Benoit, Y. Le Friec, V. Caubet-Hilloutou, and A. Claverie, Solid-State Electron. **172**, 107871 (2020).

[46] A. Calderoni, M. Ferro, D. Ielmini, and P. Fantini, IEEE Electron Device Lett. **31**(9), 1023–1025 (2010).

[47] O. Boiko, D. Drozdenko, and P. Minárik, AIP Adv. **12**(2), 025306 (2022).

[48] A. K. Jonscher, Nature **267**(5613), 673–679 (1977).

[49] B. M. Greenhoe, M. K. Hassan, J. S. Wiggins, and K. A. Mauritz, J. Polym. Sci., Part B: Polym. Phys. **54**(19), 1918–1923 (2016).

[50] A. N. Papathanassiou, I. Sakellis, and J. Grammatikakis, Appl. Phys. Lett. **91**(12), 122911 (2007).

[51] C. Liang, J. Gest, G. Leroy, and J. C. Carru, J. Appl. Phys. **114**(12), 124106 (2013).

[52] C. Cramer, S. Brunklaus, E. Ratai, and Y. Gao, Phys. Rev. Lett. **91**(26 Pt 1), 266601 (2003).

[53] R. H. Chen, L.-F. Chen, and C.-T. Chia, J. Phys.: Condens. Matter **19**(8), 086225 (2007).

[54] M. Kitao, F. Araki, and S. Yamada, Phys. Status Solidi **37**(2), K119–K121 (2006).

[55] S. M. Sze, J. Appl. Phys. **38**(7), 2951–2956 (1967).

[56] S. Habermehl and R. T. Apodaca, Appl. Phys. Lett. **86**(7), 072103 (2005).